

Engineering strong coupling with molecular coatings in optical nanocavities

Athul S. Rema,¹ Adrián E. Rubio López,¹ and Felipe Herrera^{1,2}

¹*Department of Physics, Universidad de Santiago de Chile,
Av. Victor Jara 3493, Santiago, 9170124, Chile.*

²*Millennium Institute for Research in Optics, Concepción, Chile.*

(Dated: March 19, 2026)

Quantum emitters near the surface of silver nanoparticles undergo Rabi oscillations in electronic population dynamics due to strong coupling with near-field multipole modes that are not radiative. Low-frequency nanoparticle dipole modes are radiative but do not couple strong enough to quantum emitters. These features limit the observation of strong coupling. Using macroscopic quantum electrodynamics theory within a Lorentzian pseudo-mode approximation for the non-Markovian interaction kernel, we demonstrate that by coating spherical silver nanoparticles with a thin molecular J-aggregate layer, the resulting core-shell plexciton resonance restructures the local electromagnetic vacuum at dipole-mode frequencies to enable Rabi oscillations for quantum emitters that otherwise would only undergo exponential population decay. Specifically, we show for quantum dot emitters in the near field of silver nanospheres of 20 nm radius, that weak-to-strong coupling crossovers can be induced using 2 nm J-aggregate shells. Our work demonstrates the potential of molecular aggregates to enable deep sub-wavelength structuring of the vacuum field for the observation of coherent quantum dynamics in optical nanocavities.

I. INTRODUCTION

Achieving strong coupling between a quantum emitter and a confined electromagnetic mode remains a central milestone in nanophotonics [1, 2]. In this regime, coherent energy exchange overcomes the intrinsic decay pathways of the cavity and emitter, enabling control over light-matter interactions at the nanoscale [3, 4]. Plasmonic nanocavities are natural platforms for reaching strong coupling because they concentrate optical fields into extremely small volumes [5–8]. Placing emitters in close proximity to metal structures inside sub-nanometer gaps can in principle affect the emitter orbital structure, requiring treatments that go beyond simple point-dipole approximations [9, 10]. Extreme field confinements can also be detrimental to quantum coherence, due to non-radiative population quenching into the metal structure [11–15]. Therefore, strategies to reduce emitter-metal distances without losing quantum coherence are important.

Alternative to modifying the metal-emitter distance for reaching strong coupling is to restructure the photonic environment of optical nanocavities. In this work, we propose coating a metallic nanoparticle with a highly polarizable molecular aggregate layer to restructure the local density of optical states experienced by a nearby quantum emitter. Molecular coatings can produce plexcitonic resonances due to strong interaction between molecular excitons and surface plasmons [16–20]. The optical response of the underlying nanoparticle is substantially altered if the coating material possesses a large collective oscillator strength. Strong optical absorption and the resulting anomalous dispersion in the coating can shift the boundary conditions of the local electromagnetic field, forming new resonant plexcitonic modes that are not naturally present in bare metallic structures [21].

Modeling the non-Markovian dynamics of quantum

emitters in the near field of highly-structured plexcitonic resonances requires macroscopic quantum electrodynamics theory [22, 23], which can consistently describe weak coupling phenomena (Purcell-enhanced emission) and strong coupling physics (light-matter hybridization), for realistic nanocavity structures composed of dispersive and absorptive materials. This theoretical framework was used recently to study the steady-state photon statistics of plexcitons in specialized mirror-gap geometries [24]. Here, we focus on the transient dynamics of the emitter electronic population induced by core-shell spherical nanoparticles. Standard Markovian quantum optics theory fails to fully capture the coupled emitter-nanoparticle system dynamics, due to the limitations of Markovian theory for treating broadband multi-mode nanocavity structures [25, 26].

We apply a recently developed Lorentzian kernel approximation [27] for solving the non-Markovian quantum dynamics equations that govern the emitter-nanoparticle system. This approximation becomes exact for nanocavities composed of Drude metal nanoparticles, which produce simple Lorentzian resonances in the local density of photon states [28], but can accurately solve the quantum dynamics of emitters in more complex system that involve strong photon-photon interactions between near-field modes [27]. Using this method, we demonstrate that by inserting an active molecular J-aggregate layer in the gap between the surface of a silver metal sphere and a quantum dot emitter, the electromagnetic vacuum at the emitter position is modified such that over frequency regions where Purcell-enhanced spontaneous emission is expected without the aggregate layer, Rabi oscillations of the population due to strong coupling occurs, associated with large Rabi splittings in the emission spectrum. Our work provides the first rigorous demonstration that molecular coatings can be used for engineering the quantum dynamics of dipole emitters at target frequencies,

without modifying the distance between the emitter and the metallic surface.

The rest of the article is organized as follows: Section II introduces the theoretical framework, detailing the macroscopic quantum electrodynamics formalism and the Lorentzian kernel approximation. Section III defines the plexcitonic nanoparticle system, comparing the material permittivities and hybridization mechanisms of the bare and coated silver nanospheres. Section IV presents our main results, first evaluating the restructured spectral density of the electromagnetic vacuum, and then analyzing the resulting time-domain population dynamics and coherence spectra. Finally, Section V summarizes our findings and provides an outlook on experimental feasibility and future theoretical extensions.

II. THEORETICAL FRAMEWORK

A. Macroscopic QED and the memory kernel

We treat light–matter interaction using macroscopic QED theory [22, 29]. The dipole emitter is described as a charge distribution and the cavity is defined by the confined near field of an arbitrary material structure with local linear permittivity $\epsilon(\omega)$ and permeability $\mu(\omega)$. The total Hamiltonian derived from first principles can be written as [23, 27, 28, 30, 31]

$$\hat{\mathcal{H}} = \hat{\mathcal{H}}_{\text{dip}} + \hat{\mathcal{H}}_{\text{f}} + \hat{\mathcal{H}}_{\text{int}}, \quad (1)$$

with the qubit described by $\hat{\mathcal{H}}_{\text{dip}} = \hbar\omega_g|g\rangle\langle g| + \hbar\omega_e|e\rangle\langle e|$, where $|g\rangle$ and $|e\rangle$ are the ground and excited dipole states, with frequencies ω_g and ω_e , respectively. The quantized near field is described by

$$\hat{\mathcal{H}}_{\text{f}} = \int_0^\infty d\omega \hbar\omega \hat{a}^\dagger(\omega)\hat{a}(\omega), \quad (2)$$

with field operators satisfying bosonic commutation relations $[\hat{a}(\omega), \hat{a}^\dagger(\omega')] = \delta(\omega - \omega')$ and $[\hat{a}(\omega), \hat{a}(\omega')] = 0$. These are defined from the fundamental field modes in macroscopic QED through an emitter-centered orthonormalization procedure introduced in Ref. [23].

The light–matter interaction Hamiltonian is given by

$$\hat{\mathcal{H}}_{\text{int}} = \int_0^\infty d\omega g(\omega) \hat{d}^{(+)}\hat{a}(\omega) + \text{H.c.}, \quad (3)$$

with the coupling function given by

$$g(\omega) = \sqrt{\frac{\hbar\omega^2}{\pi\epsilon_0 c^2}} \mathbf{e}_\alpha \cdot \mathfrak{S}[\overset{\leftrightarrow}{\mathbf{G}}(\mathbf{r}_0, \mathbf{r}_0, \omega)] \cdot \mathbf{e}_\alpha, \quad (4)$$

where $\overset{\leftrightarrow}{\mathbf{G}}(\mathbf{r}_0, \mathbf{r}_0, \omega)$ is the dyadic Green's tensor [32] evaluated at the emitter position \mathbf{r}_0 for dipole orientation \mathbf{e}_α . The dipole operator is $\hat{d}^{(+)} = d_{eg}|e\rangle\langle g|$,

with $d_{eg} = \langle e|\hat{d}|g\rangle$ the transition dipole moment. Equation (3) is in the rotating-wave approximation. Operating within this approximation allows us to construct a semi-analytical solution for the non-Markovian dynamics, which is useful for modeling structured nanophotonic environments [27].

We use the following Wigner–Weisskopf ansatz for the dipole-photon state $|\psi(t)\rangle$,

$$|\psi(t)\rangle = C_{g0}(t)|g\rangle|\{0\}\rangle + C_{e0}(t)e^{-i\omega_e t}|e\rangle|\{0\}\rangle + \int_0^\infty d\omega C_{g1}(\omega, t)e^{-i\omega t}|g\rangle|\{\mathbf{1}(\omega)\}\rangle, \quad (5)$$

where $|\{0\}\rangle$ is the photonic vacuum and $|\{\mathbf{1}(\omega)\}\rangle = \hat{a}^\dagger(\omega)|\{0\}\rangle$ is the one-photon eigenstate of $\hat{\mathcal{H}}_{\text{f}}$. $C_{e0}(t)$ is the dipole excited-state amplitude and $C_{g1}(\omega, t)$ is the single-photon wavefunction [33, 34].

We consider spontaneous emission from an initially excited emitter with no photons present. In the absence of external driving, the ground-state amplitude $C_{g0}(t)$ decouples from the remaining system dynamics [27] (see Appendix C). The relevant initial conditions governing the evolution are therefore $C_{e0}(0) = 1$ and $C_{g1}(\omega, 0) = 0$.

Projecting the Schrödinger equation onto the basis states yields an integro-differential equation (IDE) for the dipole excitation amplitude (see derivation in Appendix C)

$$\dot{C}_{e0}(t) = - \int_0^t dt' \mathcal{K}(t-t') C_{e0}(t'), \quad (6)$$

with the evolution governed by the delay kernel

$$\mathcal{K}(t-t') = \int_0^\infty d\omega \mathcal{K}(\omega) e^{-i(\omega-\omega_e)(t-t')}. \quad (7)$$

The kernel spectrum $\mathcal{K}(\omega) = d_{eg}^2|g(\omega)|^2/\hbar^2$ (units of Hz) is sometimes referred to as spectral density in the literature. It encodes the full broadband electromagnetic response at the emitter location and is computed exactly from the dyadic Green's function. The single-photon amplitude follows by direct integration,

$$C_{g1}(\omega, t) = -i \int_0^t dt' \sqrt{\mathcal{K}(\omega)} C_{e0}(t') e^{i(\omega-\omega_e)t'}. \quad (8)$$

B. Lorentzian kernel approximation

Equation (6) can be solved numerically using standard integration methods [35], once the delay kernel $\mathcal{K}(\tau)$ is known. Analytical solutions are possible when the kernel in the time domain is given by a sum of exponentials [36, 37]. For a single exponential memory kernel of the form $\mathcal{K}(\tau) = A e^{-\tilde{B}\tau}$, where A is real and \tilde{B} is complex valued, the Laplace domain solution of Eq (6), $G(s) = (s + \tilde{B})/(s^2 + \tilde{B}s + A)$ inverts to [27]

$$C_{e0}(t) = e^{-\tilde{B}t/2} \left[\cos(bt) + \frac{\tilde{B}}{2b} \sin(bt) \right], \quad (9)$$

with $2b = \sqrt{4A - \tilde{B}^2}$. Qualitatively, for a kernel with large enough amplitude and a small memory decay rate ($|A| \gg |\tilde{B}|^2/4$), the parameter b is real and the system exhibits damped Rabi oscillations, a signature of strong coupling, with population lifetime $T_1 = 1/\text{Re}[\tilde{B}]$ and Rabi frequency $\Omega_R = 2\text{Re}[b]$. If the kernel amplitude is very small ($|A| \ll |\tilde{B}|^2/4$), then C_{e0} undergoes simple exponential decay from its initial amplitude, a signature of weak coupling.

The generalization of this analytical solution is worked out by writing the memory kernel as the parametric model

$$\mathcal{K}(\tau) = \sum_{j=1}^n A_j e^{(-B_j - i[\Omega_j - \omega_e])\tau}, \quad (10)$$

whose Fourier transform gives the Lorentzian expansion

$$\mathcal{K}(\omega) = \sum_{j=1}^n \frac{A_j}{\pi} \frac{B_j}{(\omega - \Omega_j)^2 + B_j^2}, \quad (11)$$

where each Lorentzian is centered at Ω_j with bandwidth $2B_j$ (FWHM) and area A_j . This expansion is used to approximate the true kernel spectrum $\mathcal{K}(\omega)$ through a fitting procedure, with (n, A_j, B_j, Ω_j) as fit parameters. When the near-field multipole expansion is converged, the exact memory kernel for the systems studied here yields exclusively positive amplitudes ($A_j > 0$). This ensures the Lorentzian decomposition acts as a proper physical pseudo-mode expansion [38, 39].

Defining $\tilde{B}_j = B_j + i(\Omega_j - \omega_e)$, the Laplace transform of the IDE with $C_{e0}(0) = 1$ yields

$$\tilde{C}_{e0}(s) = \frac{Q(s)}{P(s)}, \quad (12)$$

where $Q(s) = \prod_k (s + \tilde{B}_k)$ and $P(s) = sQ(s) + \sum_k A_k Q_k(s)$ with $Q_k(s) = \prod_{j \neq k} (s + \tilde{B}_j)$. $P(s)$ is a polynomial of degree $n+1$. Its roots $\{s_m\}$ give the time-domain solution via the residue theorem [27, 36] (see Appendix D),

$$C_{e0}(t) = \sum_m R_m e^{s_m t}. \quad (13)$$

Each pole $s_m = -\gamma_m + i\omega_m$ contributes a damped oscillation with residue weight $R_m = Q(s_m)/P'(s_m)$. The physical coupling regime is classified by the distribution of these residue weights. We define three distinct dynamic regimes: (i) Weak Coupling (WC) occurs when a single pole dominates ($|R_1| > 0.9$), resulting in monotonic exponential decay regardless of the pole's ω_m/γ_m ratio, (ii) single-mode Strong Coupling (SC) emerges when two complex-conjugate poles contribute similarly ($|R_1| \approx |R_2| \approx 0.4$ to 0.5), producing underdamped Rabi oscillations; (iii) Multi-Mode Strong Coupling (MM-SC) occurs when the local density of states is shaped by overlapping proximal resonances [40]. In this regime, the

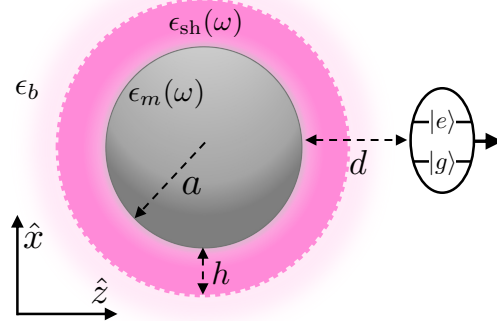


FIG. 1. Schematic of the core-shell plexcitonic nanocavity. A silver nanosphere of radius $a = 20$ nm is coated with a J-aggregate shell of thickness h and suspended in a homogeneous medium ($n_b = 1.3$, $\epsilon_b = 1.69$). A z -oriented quantum dot ($d_{eg} = 24$ D) is placed on the symmetry axis at a fixed metal-to-emitter gap of $d = 3$ nm. The coated configuration features a shell thickness of $h = 2$ nm ($\omega_{ex} = \omega_{sp}$, $f = 0.3$, $\gamma_{ex} = 50$ meV).

residue weight fragments asymmetrically across three or more poles. This structural asymmetry leads to irregular multifrequency beatings and complex multiplet spectral signatures. We visualize this spectral features by computing the excited-state coherence spectrum. The stationary single-photon spectral density is directly proportional to $\text{Im} C_{e0}(\omega) \equiv \int_0^\infty dt \text{Im}[C_{e0}(t) e^{-i\omega_e t}] e^{-i\omega t}$, as established in recent non-Markovian wavepacket treatments [27]. We use this spectrum to extract the Rabi splitting energies across all configurations.

III. PLEXCITONIC NANOPARTICLE SYSTEM

We study two nanocavity configurations for a single two-level emitter near a silver nanosphere. Figure 1 illustrates the geometry. The system is suspended in a homogeneous medium with refractive index $n_b = 1.3$. The emitter has a transition dipole moment $d_{eg} = 24$ D oriented along the z -axis. This dipole moment is representative of colloidal quantum dots [41, 42]. The emitter is placed at a fixed distance $d = 3$ nm from the metal surface. For the coated configuration, a 2 nm J-aggregate shell occupies the inner portion of the metal-emitter gap.

The silver core is described by the Drude permittivity

$$\epsilon_m(\omega) = \epsilon_\infty - \frac{\omega_p^2}{\omega(\omega + i\gamma)}, \quad (14)$$

with $\epsilon_\infty = 3.7$, plasma frequency $\omega_p = 8.55$ eV, and damping rate $\gamma = 65$ meV [21]. Mie theory places the dipolar localized surface plasmon resonance for a 20 nm sphere at $\omega_{sp} \approx 3.07$ eV, slightly red-shifted from the quasi-static Fröhlich condition ($\text{Re}[\epsilon_m] = -2\epsilon_b$) due to finite-size retardation and radiation damping.

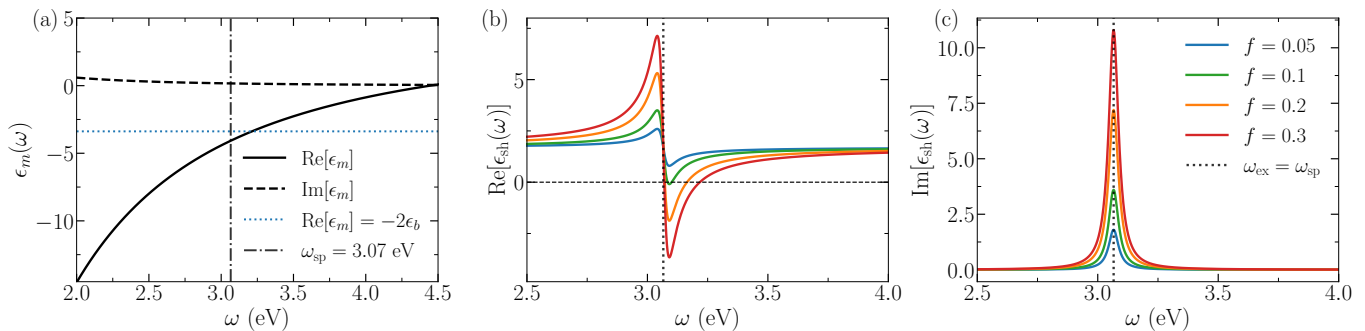


FIG. 2. Material permittivities. (a) Real (solid) and imaginary (dashed) parts of the Drude permittivity $\epsilon_m(\omega)$ of the silver core. The horizontal line marks the quasistatic Fröhlich condition $\text{Re}[\epsilon_m] = -2\epsilon_b$. The vertical dash-dotted line indicates the retarded dipole resonance $\omega_{sp} \approx 3.07$ eV for the $a = 20$ nm sphere, slightly red-shifted from the quasistatic intersection due to electrodynamic retardation. (b) Real and (c) imaginary parts of the J-aggregate shell permittivity $\epsilon_{sh}(\omega)$ for varying nominal oscillator strengths f . In both (b) and (c), the exciton is tuned to the bare plasmon resonance ($\omega_{ex} = \omega_{sp}$) with linewidth $\gamma_{ex} = 50$ meV, and the vertical dotted line marks ω_{ex} .

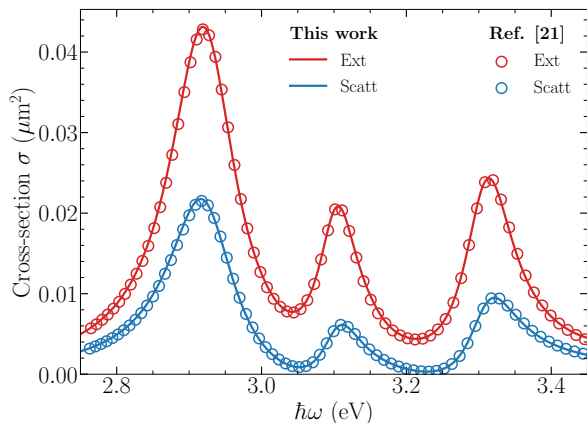


FIG. 3. Extinction and scattering cross sections of the Ag/J-aggregate core-shell nanoparticle (core radius $a = 20$ nm, shell thickness $h = 2$ nm). Solid curves represent our Lorenz-Mie calculations using the Drude core and Lorentz shell permittivities with the oscillator strength rescaling described in the text. Symbols denote results from Ref. [21]. The three peaks correspond, in order of increasing frequency, to the lower polariton, the geometric shell resonance, and the upper polariton.

The second configuration coats the silver core with a thin excitonic shell modeled as a Lorentz oscillator, with permittivity

$$\epsilon_{sh}(\omega) = \epsilon_{\infty,sh} + \frac{f \omega_{ex}^2}{\omega_{ex}^2 - \omega^2 - i\gamma_{ex}\omega}. \quad (15)$$

Following Ref. [21], we set the background permittivity $\epsilon_{\infty,sh} = 1.69$ matching the surrounding medium, shell thickness $h = 2$ nm, exciton linewidth $\gamma_{ex} = 50$ meV, and the exciton frequency ω_{ex} tuned to the bare plasmon resonance ω_{sp} to maximize hybridization. f dimensionless oscillator strength.

A subtlety arises when tuning ω_{ex} across different plasmon frequencies. At resonance, $\text{Im}[\epsilon_{sh}] = f \omega_{ex}/\gamma_{ex}$,

which scales linearly with the exciton frequency. Simply shifting ω_{ex} to track different plasmon modes would unphysically inflate the peak absorption. Following Ref. [21], we correct this by defining f at a fixed reference frequency $\omega^* = 1.8$ eV and rescaling the effective oscillator strength as $f \rightarrow f \omega^*/\omega_{ex}$ in Eq. (15). The nominal value $f = 0.3$ translates to an effective strength of $\tilde{f} \approx 0.18$ at the plasmon frequency, within reported experimental limits for cyanine dyes [43].

The critical material requirement for this coating is that $\text{Re}[\epsilon_{sh}]$ must drop below zero in a spectral window just above the exciton frequency. Any Lorentz oscillator achieves this if the oscillator strength is large enough and the linewidth is narrow. Prior quasistatic calculations established that $f \gtrsim 0.1$ with $\gamma_{ex} = 50$ meV is sufficient [21]. Molecular J-aggregates are well suited to meet this demand. Their superradiant collective transitions concentrate high oscillator strength into narrow spectral lines at room temperature [43, 44], routinely achieving $f \geq 0.3$ with exciton linewidths near $\gamma_{ex} \approx 50$ meV due to motional narrowing. Cyanine dyes such as TDBC are frequently grown as conformal thin shells directly around colloidal nanoparticles [16, 17]. Because the macroscopic oscillator strength scales with both the molecular packing density and the square of the molecular transition dipole [45], dense coherently coupled layers naturally satisfy the conditions required to achieve $\text{Re}[\epsilon_{sh}] < 0$ at visible frequencies. Transition metal dichalcogenide monolayers [46] and perovskite quantum wells [47] could also reach these conditions owing to their comparably large excitonic oscillator strengths.

Figure 2 displays the core and shell permittivities. When $f = 0.3$, $\text{Re}[\epsilon_{sh}]$ drops below zero in a spectral window just above ω_{ex} . This transient metallic character alters the macroscopic optical response of the nanoparticle. As shown in the far-field cross sections in Figure 3, the extinction and scattering spectra splits into upper and lower polariton branches separated by ~ 0.6 eV, and a third narrow peak emerges directly between them. Our

Lorenz–Mie calculations quantitatively agree with previous results for this geometry in Ref. [21]. The physical origin and near-field consequences of this intermediate feature are analyzed in the following subsection.

A. Geometric mode and the restructured vacuum

To understand the origin of the intermediate spectral feature observed in Fig. 3, we consider the plasmon hybridization framework [48]. Any nanoscale shell supports two boundary resonances: an outer sphere mode and an inner cavity (or void) mode. These hybridize into bonding and antibonding states whose splitting depends on the shell’s aspect ratio and the permittivity contrast across its interfaces [49]. For a standard dielectric shell, these hybridized modes carry minimal oscillator strength and produce no sharp optical features. The situation changes when the molecular layer has negative real part of the permittivity just above ω_{ex} , which gives the shell an effectively metallic character in that frequency window. This hybridizes the void mode into a sharp optical resonance. Because the spectral position of this resonance is governed primarily by the shell’s physical thickness and geometry rather than the metallic core, we refer to it as the geometric mode [21].

Several properties distinguish the geometric mode from the standard polariton branches. Its linewidth (FWHM ≈ 50 meV) tracks the excitonic damping γ_{ex} rather than the broader polariton linewidths, which inherit additional contributions from radiation damping and the plasmon’s multipole structure. A finite shell thickness gives it large spectral weight by concentrating surface charges almost exclusively at the outer interface.

The far-field cross sections characterize the nanoparticle’s antenna response. The near-field quantity that governs the emitter’s quantum dynamics is the imaginary part of the Green’s tensor, $\text{Im}[G_{zz}(\mathbf{r}_0, \mathbf{r}_0, \omega)]$, evaluated at the emitter position. This narrow geometric mode creates a sharp peak in $\text{Im}[G_{zz}]$ precisely where the bare metal provides only a broad, featureless spectral density. The kernel spectrum $\mathcal{K}(\omega)$ in Eq. (6) is constructed directly from this Green’s tensor via Eq. (4). We compute it using analytic Mie theory for coated spheres [50–52], with the dyadic Green’s tensor built from the exact scattering amplitudes as detailed in Appendix A. The multipole expansion is converged at $n_{\text{max}} = 60$ for the fixed center-to-dipole distance $R = 23$ nm.

IV. RESULTS

A. Coupling kernel spectrum

Figure 4 compares $\mathcal{K}(\omega)$ for the bare and coated nanospheres. The kernel for the bare sphere exhibits a hierarchy of multipole contributions that merge into a broad spectral envelope, as shown in Fig. 4(a). For

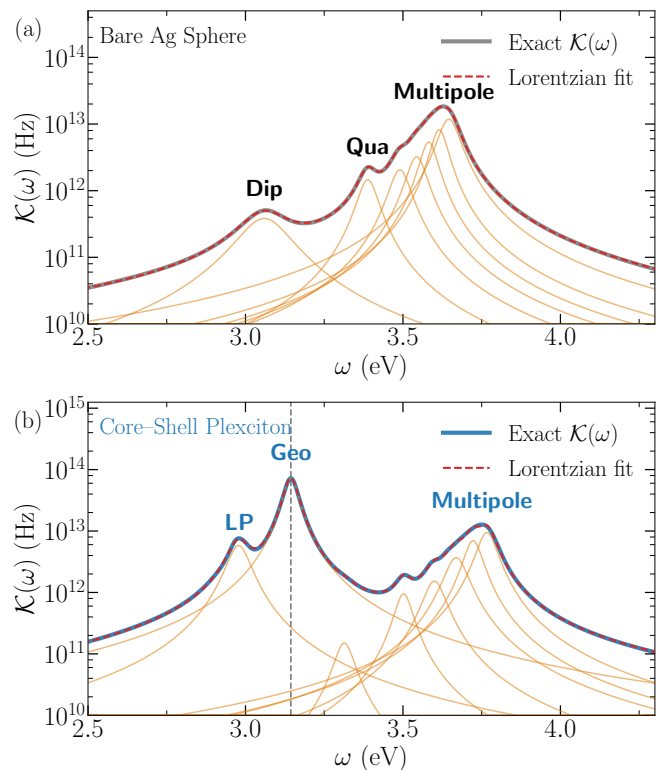


FIG. 4. Kernel spectrum $\mathcal{K}(\omega)$ on a logarithmic scale for a z -oriented quantum dot ($d_{eg} = 24$ D) placed at a fixed metal-to-emitter gap of $d = 3$ nm. (a) Spectrum for the bare Ag nanosphere of radius $a = 20$ nm. (b) Spectrum for the Ag/J-aggregate core-shell plexciton with the same core radius and a shell thickness of $h = 2$ nm. Thick solid curves (gray for the bare sphere, blue for the plexciton) represent the Mie theory calculation. Dashed red lines denote the total multi-Lorentzian fit defined in Eq. (11). Solid orange lines show the individual Lorentzian components comprising the pseudo-mode expansion. A vertical dashed line marks the frequency of the geometric mode (Geo) at 3.14 eV.

a 3 nm gap, higher-order multipoles are enhanced by the near-field weighting. The dipolar localized surface plasmon resonance at 3.06 eV carries modest spectral weight and appears as a lower-energy shoulder. Resolved quadrupolar and octupolar contributions emerge between 3.39 and 3.55 eV, while a dominant multipole complex centered near 3.65 eV carries most of the total spectral weight. These features are consistent with previous literature [42, 53]. Seven Lorentzians are needed to reproduce the bare kernel spectrum, all with positive amplitudes. This positivity is consistent with the fact that each multipole order ℓ contributes independently to the imaginary part of the Green’s tensor without cross-channel interference[54].

Fig. 4(b) shows the spectrum for the coated configuration. Eight Lorentzians with positive amplitudes are required to reproduce the fully converged spectrum. Comparing the two decompositions peak by peak reveals how the molecular shell transforms the spectral landscape.

TABLE I. Strong coupling criterion evaluated at isolated kernel peaks. A_j is the total spectral weight and B_j is the half-width of the dominant Lorentzian near ω_e . Strong coupling requires the unitless single-peak ratio $2A_j/B_j^2 > 1$ [27].

ω_e (eV)	System	Peak	A_j (meV ²)	B_j (meV)	$2A_j/B_j^2$
2.98 (LP)	Bare Ag	—	—	—	$\ll 1$
2.98 (LP)	Core-shell	$j=1$	440	36.6	0.66
3.14 (Geo)	Bare Ag	—	—	—	$\ll 1$
3.14 (Geo)	Core-shell	$j=2$	3717	24.8	12.10
3.64 (UV)	Bare Ag	$j=7$	854	34.8	1.41
3.64 (UV)	Core-shell overlap	—	—	—	—

The dipolar contribution redshifts by about 0.08 eV from its bare sphere position to form the lower polariton near 2.98 eV. According to the plasmon hybridization picture [21], this mode corresponds to the bonding combination of the plasmon and exciton, with strong surface charge density at both the inner and outer shell interfaces. This hybridization-enhanced charge redistribution accounts for the nearly sevenfold increase in near-field spectral weight relative to the bare sphere dipolar mode. Nevertheless, its single-Lorentzian criterion ratio remains below unity ($2A/B^2 \approx 0.66$), indicating that coherent exchange at this frequency is mediated by the full plexcitonic continuum rather than by this mode in isolation.

The geometric mode emerges as the single most dominant peak in the spectrum at 3.14 eV, located between the polariton branches. This feature has no counterpart in the bare sphere kernel. The exciton linewidth sets its half-width to 24.8 meV rather than the broad metallic damping. Because the emitter is placed only 1 nm from the outer shell surface, it couples intensely to a manifold of high-order multipole fields that constructively sum at this frequency. The resulting spectral weight ($A \approx 3717$ meV²) yields a single-Lorentzian strong coupling ratio of 12.1, placing the geometric mode well into the strong coupling limit.

The intermediate multipole region between 3.3 and 3.6 eV is strongly suppressed in the coated system. These modes are detuned from the exciton and do not hybridize with it directly. Instead, the negative permittivity window of the shell repels them, acting as a spectral barrier that extends from just above the exciton frequency to roughly 3.4 eV.

The dominant multipole complex centered near 3.65 eV in the bare sphere shifts upward to the 3.72–3.77 eV range in the coated system. This displacement cannot be explained by a simple two-oscillator polariton model because these high-order modes are far detuned from the exciton frequency. The region instead merges contributions from the upper polariton with the modified multipole tail pushed upward by the negative permittivity window.

Table I summarizes the strong coupling criterion evaluated at isolated peaks for both configurations. The

coated kernel satisfies the criterion at the geometric mode frequency, while the bare sphere at the same frequency distributes its spectral weight over a much wider bandwidth and does not reach strong coupling. Conversely, the bare sphere satisfies the criterion at the near-UV multipole complex. Strong coupling is therefore not absent from the uncoated system but is simply confined to higher energies.

B. Quantum Emitter dynamics

Figure 5 shows the population dynamics $|C_{e0}(t)|^2$ from the Laplace residues [Eq. (13)] and the coherence spectrum $\text{Im} C_{e0}(\omega)$.

The density maps reveal how the molecular coating reshapes the electromagnetic vacuum across the full spectrum. For the bare sphere, the population map [Fig. 5(b)] shows two distinct dynamical regions. Above approximately 3.4 eV, clear oscillatory fringes indicate coherent population exchange with the near-UV multipole modes, with the tightest fringe spacing near 3.6 eV where the spectral weight is largest. Below 3.4 eV, the population decays monotonically without revivals, transitioning from moderate Purcell-enhanced decay near the dipolar LSPR at 3.06 eV to negligible coupling at lower frequencies. The coherence spectrum [Fig. 5(c)] shows a single avoided crossing near 3.6 eV, while below 3.4 eV the spectrum follows the emitter frequency, consistent with previous studies of emitters near bare metallic surfaces [13].

The coated system presents a qualitatively different picture. The population map [Fig. 5(d)] shows coherent oscillations across a much broader range of frequencies. From 2.8 to 3.3 eV, pronounced oscillatory fringes appear where the bare sphere showed only monotonic decay. The tightest fringe spacing occurs near the geometric mode at 3.14 eV, where the population collapses within approximately 10 fs. A second region of oscillations persists near 3.7–3.8 eV. Between these two regions, from roughly 3.3 to 3.6 eV, the population decays without revivals, reflecting the suppressed spectral density in the $\text{Re}[\epsilon_{\text{sh}}] < 0$ spectral gap. The coherence map [Fig. 5(e)] reveals the spectral origin of this behavior. Two distinct regions of coherent exchange emerge. Near 3.75 eV, an isolated anti-crossing appears with well-separated upper and lower branches. The visible range from roughly 2.8 to 3.3 eV is qualitatively different. When an emitter sweeps through a single well-isolated near-field resonance, the coherence spectrum avoided crossing [55]. If the geometric mode and the lower polariton acted as independent near-field channels, each would produce its own avoided crossing centered at 2.98 eV and 3.14 eV respectively. Instead, the spectral branches merge into a continuous multi-branch structure, indicating that these two plexcitonic features overlap in the near field to form a coupled multi-mode continuum as experienced by the emitter.

Figure (6) compares two frequency cuts of Fig. 5 at ω_e values 3.14 eV and 2.98 eV.

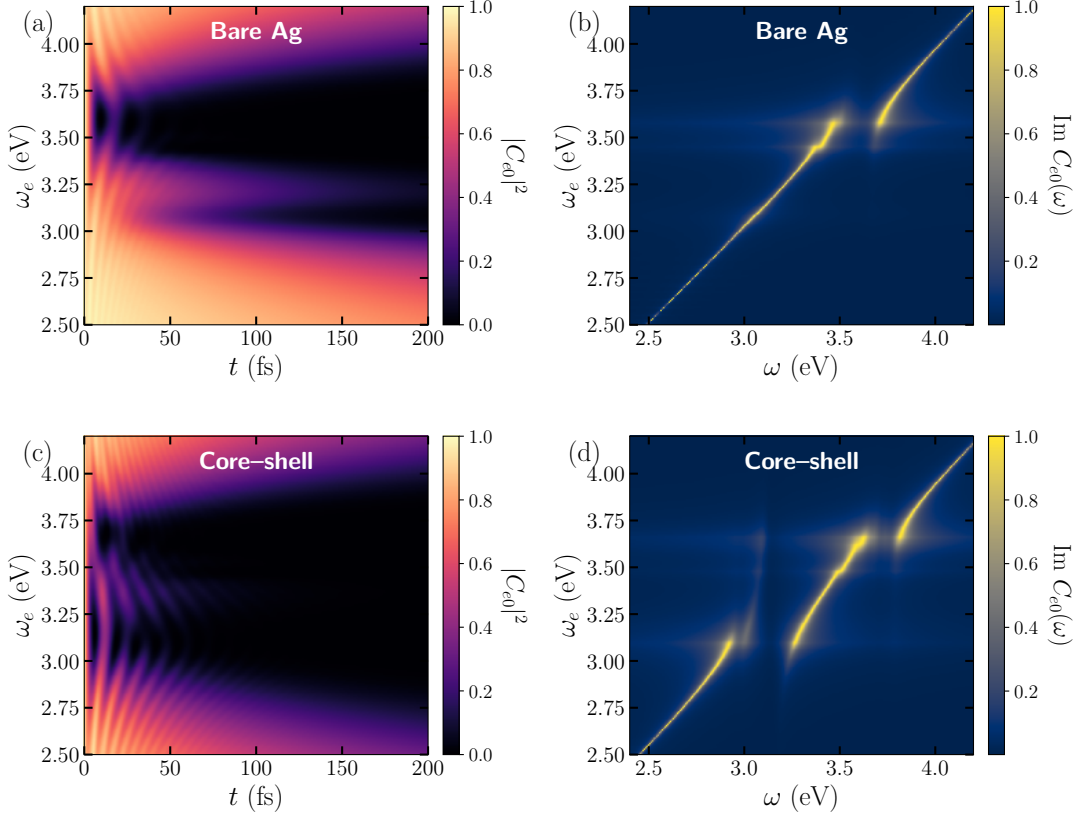


FIG. 5. Broadband emitter dynamics and coherence spectra as a function of transition frequency ω_e at a fixed gap of 3 nm. (a) Excited-state population dynamics $|C_{e0}(t)|^2$ for the bare silver nanosphere at different dipole frequencies ω_e . (b) Normalized excited-state coherence spectra for the bare sphere, exhibiting a single avoided crossing near the Near-UV multipole at 3.65 eV. (c) Population dynamics $|C_{e0}(t)|^2$ for the coated core-shell system at different dipole frequencies ω_e . (d) Coherence spectra for the core-shell system. The molecular coating induces two distinct regions of coherent exchange: a blue-shifted multipole near 3.75 eV, and a merged multi-branch avoided crossing in the visible spectrum. This merged feature demonstrates that the geometric mode (3.14 eV) and the lower polariton (2.98 eV) act collectively as a dense, overlapping multi-mode continuum rather than independent modes.

1. Geometric mode: three-level hybridization

At $\omega_e = 3.14$ eV, the bare sphere places the emitter in a spectral valley. A single pole dominates ($|R_1| = 0.95$), yielding simple exponential decay with a Purcell factor $F_P \approx 578$. The core-shell system produces a different response. Because the geometric mode carries significant spectral weight and is only 166 meV from the lower polariton, the emitter simultaneously hybridizes with both features. The residue weight distributes across three poles with nearly balanced amplitudes ($|R_1| = 0.45$, $|R_2| = 0.29$, $|R_3| = 0.25$), giving three-level hybridization.

The coherence spectrum in Fig. 6(b) resolves a triplet with peaks at 2.94, 3.01, and 3.29 eV. This spectral structure encodes two distinct energy scales. The total span of $\Omega_R = 345$ meV between the outermost peaks sets the fast carrier oscillation period of 12 fs. The two lower peaks are separated by only 69 meV, producing a slow 60 fs envelope modulation superimposed on the fast exchange.

The near-symmetric distribution of residue weight enables deep destructive interference, driving the excited-state population to zero at 7 fs before the onset of dephasing [Fig. 6(a)].

The two energy scales have a transparent physical origin. The 345 meV total splitting reflects the emitter's simultaneous coupling to the geometric mode and the lower polariton, whose combined spectral weight spans this energy window. The 69 meV fine splitting arises from the internal structure of the lower polariton manifold as seen by an emitter tuned to the geometric mode frequency. The dominant population oscillation frequency extracted from the pole analysis ($2\omega_1 = 290$ meV) differs from the photonic splitting ($\Omega_R = 345$ meV), reflecting the redistribution of spectral weight characteristic of multi-mode coupling. In a clean single-mode system these two quantities coincide; their divergence here quantifies the degree of multi-mode character.

TABLE II. Dominant poles $s_m = -\gamma_m + i\omega_m$, residue weights $|R_m|$, and Purcell factors F_P (evaluated for the bare sphere) at four representative emitter frequencies. $2\omega_1$ is the dominant population oscillation frequency from the pole analysis and Ω_R is the photonic Rabi splitting measured from the peak-to-peak separation in the coherence spectrum. In single-mode strong coupling these two quantities converge; their divergence diagnoses multi-mode character. SC: strong coupling; WC: weak coupling; MM-SC: multi-mode strong coupling.

ω_e (eV)	System	γ_1 (meV)	ω_1 (meV)	$ R_1 , R_2 , R_3 $	$2\omega_1$ (meV)	Ω_R (meV)	Regime
2.98	Bare ($F_P \approx 551$)	2.9	23	0.96	—	—	WC
2.98	Coated	10.0	117	0.67, 0.25, 0.07	234	372	MM-SC
3.14	Bare ($F_P \approx 578$)	5.0	25	0.95	—	—	WC
3.14	Coated	14.4	145	0.45, 0.29, 0.25	290	345	MM-SC
3.63	Bare	16.2	108	0.51, 0.21, 0.15	216	225	SC
3.63	Coated	24.8	6	0.33, 0.27, 0.25	—	196	MM-SC
3.75	Bare ($F_P \approx 1717$)	7.9	64	0.76	—	—	WC
3.75	Coated	12.9	109	0.60, 0.14, 0.13	218	207	SC

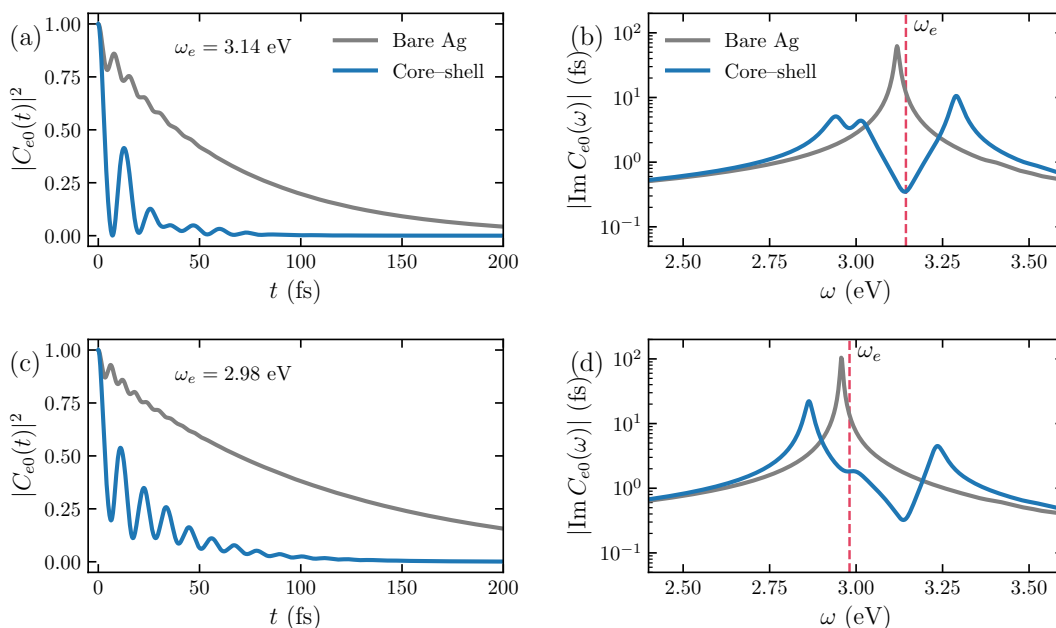


FIG. 6. Quantum emitter dynamics at the two visible-range strong coupling channels created by the molecular coating at a fixed 3 nm metal-to-emitter gap. The bare silver sphere (gray) is compared with the core-shell plexciton (blue). (a, b) Excited-state population and coherence spectrum $|\text{Im} C_{e0}(\omega)|$ (in fs) for an emitter tuned to the geometric mode frequency ($\omega_e = 3.14$ eV). Three resolved peaks form a coherence triplet spanning 345 meV, with an intra-triplet fine splitting of 69 meV between the two lower hybrid states. (c, d) Population and coherence spectrum for an emitter tuned to the lower polariton frequency ($\omega_e = 2.98$ eV). Two peaks separated by 372 meV confirm an asymmetric doublet. The vertical crimson line marks ω_e in each coherence panel. Dynamics at higher-energy multipole frequencies are visible in the 2D maps of Fig. 5 and quantified in Table II.

2. Lower polariton: asymmetric doublet

At $\omega_e = 2.98$ eV, the bare sphere interacts only with the weak tail of the dipolar LSPR ($F_P \approx 551$), and a single pole carries 96% of the residue weight. The coated system drives the emitter into strong coupling, but with a character distinct from the geometric mode channel. The residue weight fragments asymmetrically across two primary poles ($|R_1| = 0.67$, $|R_2| = 0.25$), with the third

pole contributing only 7%.

The coherence spectrum in Fig. 6(d) shows a clean doublet at 2.86 and 3.24 eV, separated by $\Delta_{\text{ph}} = 372$ meV. This photonic splitting is notably larger than the geometric mode's total splitting (345 meV), despite the lower polariton possessing far less intrinsic spectral weight ($A = 440$ versus 3717 meV²). The apparent paradox is resolved by recognizing that the upper hybrid-state peak at 3.24 eV is pulled to higher energy by the strong spec-

tral tail of the adjacent geometric mode. The 372 meV splitting therefore measures not the LP coupling strength alone, but the effective spectral span of the emitter's interaction with the entire plexcitonic continuum as seen from the LP frequency. The failure of the single-peak criterion ($2A/B^2 = 0.66$) at this frequency confirms that the coherent exchange is not an isolated two-level phenomenon but is instead mediated by the surrounding spectral density.

The residue asymmetry has a direct dynamical consequence. Unlike the geometric mode channel, where the near-balanced weight allows the population to reach zero, the 0.67 versus 0.25 imbalance prevents full destructive interference. The excited-state population drops only to a minimum near 0.2 before exhibiting pronounced multi-frequency beating [Fig. 6(c)]. The dominant pole yields a population oscillation frequency of $2\omega_1 = 234$ meV, which diverges significantly from the photonic splitting (372 meV). This large discrepancy, combined with the single-peak criterion failure, provides the clearest quantitative signature of continuum-mediated multi-mode coupling in the system.

V. CONCLUSIONS AND OUTLOOK

We adopted a recently developed Lorentzian approximation method for mapping the non-Markovian light-matter interaction kernel that describes the electronic dynamics of a quantum emitter interacting with an optical nanocavity field. The method decomposes the coupling kernel into a set of Lorentzian pseudo-modes, from which closed-form analytical expressions for the excited-state population and the emitted photon coherence can be derived [27]. The method is particularly useful for modeling complex nanophotonic environments where the local density of optical states exhibits sharp, highly structured spectral features, including mode-coupled phenomena such as Fano resonances.

It is shown that by coating a silver metal sphere with a thin molecular J-aggregate layer (core-shell structure), the near-field electromagnetic vacuum of the nanoparticle changes significantly such that a quantum emitter that would only undergo Purcell-enhanced spontaneous emission without coating, becomes strongly coupled and experiences Rabi oscillations with a multi-mode splitting spectrum. The distance nanoparticle-emitter distance remains unchanged. This weak-coupling to strong-

coupling crossover occurs due to plasmon-exciton hybridization within the core-shell structure [21], which spectrally modifies the local density of optical states. The negative real part of J-aggregate permittivity gives metallic character to the molecular shell enabling the formation of geometric resonances to which quantum emitters can strongly couple, over a frequency region where the bare metal nanoparticle does not support strong coupling.

The system studied here is within reach of current technology. Conformal J-aggregate shells with the required oscillator strengths are routinely deposited around colloidal nanoparticles at room temperature [16, 17, 43, 44]. DNA origami scaffolds [56] and cucurbituril molecular spacers [7] provide the sub-nanometer positional control needed to place individual solid-state emitters at prescribed distances. The predicted population beatings occur on timescales of ~ 10 fs, accessible to ultrafast pump-probe and time-resolved measurements [6, 18, 57]. The observation of the predicted triplet spectral feature spanning ~ 350 meV due to strong coupling with plasmon-exciton modes at visible frequencies should be straightforward.

Molecular aggregate coating layers can be used to modify the electromagnetic vacuum for other nanoparticle geometries, such as nanoparticle-on-mirror configurations, plasmonic dimers, and tip-enhanced geometries. The theoretical framework we used is completely general and can be applied for studying arbitrary nanocavity configurations provided that Green's dyadic tensor is known. Molecular coatings can therefore become valuable design tools for engineering photonic reservoirs of optical nanocavities to enable new types of chemical reactions [58–60], nanoscale energy transfer platforms [61] and nanoscale quantum control schemes [62].

ACKNOWLEDGMENTS

We thank Tomasz Antosiewicz for sharing data from Ref. [21] for validation. A.S.R. received support from USACH Excellence Graduate Scholarship. A.E.R.L. is supported by ANID-Fondecyt Iniciación No. 11250638. F.H. is supported by ANID-Fondecyt Regular Grant No. 1221420. This work was also supported by the Air Force Office of Scientific Research under Award No. FA9550-22-1-0245 and ANID-Millennium Science Initiative Program No. ICN17.012.

Appendix A: Lorenz–Mie theory and the Green's tensor

This appendix outlines the derivation of the kernel spectrum $\mathcal{K}(\omega)$ from classical Mie scattering theory. We construct the dyadic Green's tensor at the emitter position directly from the exact Mie coefficients of the coated sphere, which yields the coupling kernel via Eq. (4).

1. Mie coefficients for the coated sphere

To avoid notational conflict with the standard transverse magnetic Mie coefficients a_n , in this appendix we denote the radius of the metallic core as R_1 (corresponding to a in the main text). The core is coated with a concentric shell of thickness h , yielding an outer radius of $R_2 = R_1 + h$. The entire structure is embedded in an unbounded medium. The three regions have permittivities ϵ_j and wavenumbers $k_j = \omega\sqrt{\epsilon_j}/c$ ($j = 1, 2, 3$ for core, shell, exterior); all media are non-magnetic. The Lorenz–Mie scattering coefficients for this geometry are [51]

$$a_n = \frac{m_2 \psi'_n(k_3 R_2) - \psi_n(k_3 R_2) \mathcal{A}_n}{m_2 \xi'_n(k_3 R_2) - \xi_n(k_3 R_2) \mathcal{A}_n}, \quad (\text{A1})$$

where $m_j = k_j/k_3$ is the relative refractive index of region j , and $\psi_n(x) = x j_n(x)$, $\xi_n(x) = x h_n^{(1)}(x)$ are Riccati–Bessel functions. The effective logarithmic derivative $\mathcal{A}_n \equiv \mathcal{A}_n(m_2 k_3 R_2)$ incorporates the effect of the core:

$$\mathcal{A}_n = \frac{\psi'_n(m_2 k_3 R_2) - A_n^c \chi'_n(m_2 k_3 R_2)}{\psi_n(m_2 k_3 R_2) - A_n^c \chi_n(m_2 k_3 R_2)}, \quad (\text{A2})$$

with $\chi_n(x) = -x y_n(x)$ and the core ratio

$$A_n^c = \frac{m_2 \psi_n(m_2 k_3 R_1) \psi'_n(m_1 k_3 R_1) - m_1 \psi'_n(m_2 k_3 R_1) \psi_n(m_1 k_3 R_1)}{m_2 \chi_n(m_2 k_3 R_1) \psi'_n(m_1 k_3 R_1) - m_1 \chi'_n(m_2 k_3 R_1) \psi_n(m_1 k_3 R_1)}. \quad (\text{A3})$$

The TE (magnetic) Mie coefficient b_n follows from the same expressions with the replacement $m_j \rightarrow 1/m_j$ [51]. Far-field cross sections are

$$\sigma_{\text{ext}} = \frac{2\pi}{k_3^2} \sum_{n=1}^{\infty} (2n+1) \text{Re}[a_n + b_n], \quad (\text{A4})$$

$$\sigma_{\text{sca}} = \frac{2\pi}{k_3^2} \sum_{n=1}^{\infty} (2n+1) (|a_n|^2 + |b_n|^2). \quad (\text{A5})$$

2. Green's tensor and the kernel spectrum

The electromagnetic dyadic Green's tensor for the multilayered sphere can be constructed using the scattering superposition method [52, 63]. The total tensor is separated into a free-space component and a scattering correction. The scattering correction is expanded in vector spherical harmonics, with coefficients determined by boundary matching at each interface. When both the source and the field are located in the exterior region, the transverse magnetic (TM) and transverse electric (TE) scattering amplitudes of the Green's tensor reduce directly to the negative of the standard Mie coefficients, $-a_n(\omega)$ and $-b_n(\omega)$, respectively [64]. This exact equivalence forms the central link between macroscopic scattering theory and the local electromagnetic environment experienced by the quantum emitter.

For a z -oriented (radial) dipole located on the symmetry axis at a distance $R = R_1 + d$ from the sphere center, only the $m = 0$, TM terms of the multipole expansion survive [52, 64]. The scattering part of G_{zz} at the coincident point $\mathbf{r} = \mathbf{r}' = R \hat{z}$ simplifies to:

$$G_{s,zz}(R, R)|_{\theta=0} = -\frac{ik_3}{4\pi} \sum_{n=1}^{\infty} (2n+1) \frac{n(n+1)}{(k_3 R)^2} a_n [h_n^{(1)}(k_3 R)]^2. \quad (\text{A6})$$

The total Purcell factor for a radially oriented dipole follows from the imaginary part of the full (free-space plus scattering) Green's tensor [64]:

$$\frac{\Gamma_{\perp}}{\Gamma_0} = 1 - \frac{3}{2} \sum_{n=1}^{\infty} n(n+1)(2n+1) \text{Re} \left[a_n \left(\frac{h_n^{(1)}(k_3 R)}{k_3 R} \right)^2 \right]. \quad (\text{A7})$$

This classical Purcell enhancement is proportional to the projected local density of optical states (LDOS), providing the direct physical link between the macroscopic antenna properties and the quantum memory kernel. The kernel spectrum entering the IDE (6) is therefore defined directly from this exact Green's tensor as:

$$\mathcal{K}(\omega) = \frac{d_{eg}^2 \omega^2}{\pi \hbar \epsilon_0 c^2} \Im[G_{s,zz}(R, R; \omega)], \quad (\text{A8})$$

which is evaluated numerically by summing Eq. (A6) over multipole orders $n = 1, \dots, n_{\max}$. We use $n_{\max} = 60$, which provides convergence at the extreme near-field fixed center-to-center distance $R = a + d = 23$ nm.

Appendix B: Lorentzian fit parameters

Tables III and IV list the parameters of the multi-Lorentzian expansion [Eq. (11)] used to fit the kernel spectrum $\mathcal{K}(\omega)$ for each configuration.

For the bare Ag sphere, seven Lorentzians are needed, all with positive amplitudes. The lowest-frequency term ($j = 1$, $\Omega_1 \approx 3.06$ eV) corresponds to the dipolar LSPR; terms $j = 2$ –5 capture the resolved quadrupolar, octupolar, and higher multipole contributions in the 3.39–3.55 eV range; and the dominant multipole complex near 3.65 eV is described by terms $j = 6$ –7. All amplitudes are positive, consistent with the absence of cross-channel interference: each multipole order ℓ contributes independently to $\text{Im}[G_{zz}]$.

For the core-shell system ($f = 0.3$), eight Lorentzians are needed to capture the fully converged spectrum. The lower polariton is captured primarily by term $j = 1$ near 2.98 eV. The geometric mode at $\omega_{\text{geo}} \approx 3.14$ eV appears as the single dominant term ($j = 2$), carrying the largest spectral weight in the entire fit. An isolated intermediate multipole ($j = 3$) and the upper-polariton/multipole complex ($j = 4$ –8) complete the decomposition, all with positive amplitudes.

TABLE III. Lorentzian fit parameters for the bare Ag sphere ($a = 20$ nm, $d = 3$ nm). $n = 7$ terms, all with positive amplitudes.

j	Ω_j (eV)	B_j (eV)	A_j (meV ²)
1	3.0596	0.0828	65.6
2	3.3883	0.0321	97.2
3	3.4903	0.0336	142.7
4	3.5435	0.0319	212.7
5	3.5820	0.0282	311.9
6	3.6151	0.0273	463.9
7	3.6455	0.0348	854.1

TABLE IV. Lorentzian fit parameters for the Ag/J-aggregate core-shell ($a = 20$ nm, $h = 2$ nm, $f = 0.3$, $d = 3$ nm). The fit utilizes $n = 8$ positive-amplitude terms. The geometric mode ($j = 2$) dominates the visible spectrum.

j	Ω_j (eV)	B_j (eV)	A_j (meV ²)
1	2.9782	0.0366	439.5
2	3.1441	0.0248	3717.2
3	3.3136	0.0305	9.5
4	3.5022	0.0275	54.2
5	3.5999	0.0353	111.6
6	3.6690	0.0371	282.3
7	3.7228	0.0298	428.8
8	3.7665	0.0320	625.4

Appendix C: Integro-differential equation and stationary photon spectrum

This appendix outlines the derivation of the integro-differential equation for the excited-state amplitude [Eq. (6)] and the stationary single-photon spectrum used to define the strong coupling criterion [27].

1. Derivation of the IDE

Inserting the Wigner–Weisskopf ansatz [Eq. (5)] into the time-dependent Schrödinger equation $i\hbar\partial_t|\psi\rangle = \hat{\mathcal{H}}|\psi\rangle$ and projecting onto the basis states yields a system of coupled differential equations for the amplitudes. Formally integrating the single-photon amplitude $C_{g1}(\omega, t)$ with the initial condition $C_{g1}(\omega, 0) = 0$ yields

$$C_{g1}(\omega, t) = -i \int_0^t dt' \sqrt{\mathcal{K}(\omega)} C_{e0}(t') e^{i(\omega - \omega_e)t'}, \quad (\text{C1})$$

where $\sqrt{\mathcal{K}(\omega)} = d_{eg} |g(\omega)|/\hbar$. Substituting this formal solution back into the equation of motion for $C_{e0}(t)$ directly yields the integro-differential equation

$$\dot{C}_{e0}(t) = - \int_0^t dt' \mathcal{K}(t-t') C_{e0}(t'), \quad (\text{C2})$$

with the memory kernel $\mathcal{K}(t-t') = \int_0^\infty d\omega \mathcal{K}(\omega) e^{-i(\omega - \omega_e)(t-t')}$. This establishes Eqs. (6) and (7) of the main text.

2. Stationary spectrum and strong coupling criterion

The stationary single-photon spectrum $|C_{g1}^\infty(\omega)|^2$ determines the presence of Rabi splitting. Taking the limit $t \rightarrow \infty$ in Eq. (C1) produces an integral that is exactly the Laplace transform of $C_{e0}(t)$ evaluated at $s = -i\delta$, where $\delta = \omega - \omega_e$:

$$C_{g1}^\infty(\delta) = -i\sqrt{\mathcal{K}(\delta)} \tilde{C}_{e0}(-i\delta) = -i\sqrt{\mathcal{K}(\delta)} \frac{Q(-i\delta)}{P(-i\delta)}, \quad (\text{C3})$$

using the rational form $\tilde{C}_{e0}(s) = Q(s)/P(s)$ derived in Appendix D.

For a single Lorentzian kernel centered at the emitter frequency ($\Omega_1 = \omega_e$, so $\tilde{B} = B$), the polynomials are $Q(s) = s + B$ and $P(s) = s^2 + Bs + A$. The stationary photon intensity simplifies to

$$|C_{g1}^\infty(\delta)|^2 = \mathcal{K}(\delta) \frac{\delta^2 + B^2}{\delta^4 + (B^2 - 2A)\delta^2 + A^2}. \quad (\text{C4})$$

This spectrum exhibits a local minimum at $\delta = 0$ (a Rabi doublet) when the curvature of the denominator at the origin is negative, which requires $B^2 - 2A < 0$. Recalling that $A = \int d\omega \mathcal{K}(\omega)$ is the total spectral weight of the mode and $2B = \Gamma_{\mathcal{K}}$ is its full width at half maximum, the splitting condition $2A > B^2$ translates directly to the strong coupling criterion discussed in Ref. [27]

$$2 \int d\omega \mathcal{K}(\omega) > (\Gamma_{\mathcal{K}}/2)^2. \quad (\text{C5})$$

Appendix D: Laplace transform solution of the IDE

This appendix gives the explicit Laplace-domain solution of the integro-differential equation (6) for a kernel modeled as a sum of n Lorentzians [Eq. (11)].

1. General n -Lorentzian kernel

With the multi-exponential memory kernel from Eq. (10), the IDE for the excited-state amplitude $y(t) \equiv C_{e0}(t)$ reads

$$\dot{y}(t) = - \int_0^t d\tau \sum_{j=1}^n A_j e^{-\tilde{B}_j\tau} y(t-\tau), \quad (\text{D1})$$

where $\tilde{B}_j = B_j + i(\Omega_j - \omega_e)$ and $y(0) = 1$. Taking the Laplace transform and applying the convolution theorem gives

$$sY(s) - 1 = - \sum_{j=1}^n \frac{A_j}{s + \tilde{B}_j} Y(s), \quad (\text{D2})$$

which can be solved algebraically:

$$Y(s) = \frac{Q(s)}{P(s)}, \quad (\text{D3})$$

where the numerator polynomial is

$$Q(s) = \prod_{k=1}^n (s + \tilde{B}_k), \quad (\text{D4})$$

and the denominator polynomial is

$$P(s) = sQ(s) + \sum_{k=1}^n A_k Q_k(s), \quad (\text{D5})$$

with $Q_k(s) = \prod_{j \neq k} (s + \tilde{B}_j)$. The polynomial $P(s)$ has degree $n + 1$, so the system has $n + 1$ poles.

The time-domain solution is obtained by partial-fraction decomposition. Let $\{s_m\}_{m=1}^{n+1}$ denote the roots of $P(s)$. If all roots are simple (no degeneracies), the residue theorem gives [36]

$$C_{e0}(t) = \sum_{m=1}^{n+1} \frac{Q(s_m)}{P'(s_m)} e^{s_m t}, \quad (\text{D6})$$

where $P'(s) = dP/ds$. This is Eq. (13) of the main text. Each pole $s_m = -\gamma_m + i\omega_m$ contributes an exponentially damped oscillation at frequency ω_m with decay rate γ_m . Complex-conjugate pairs with $|\omega_m| > \gamma_m$ produce damped Rabi oscillations; purely real poles (or pairs with $|\omega_m| \ll \gamma_m$) produce exponential decay.

2. Explicit form for $n = 1$

For a single Lorentzian at $\Omega_1 = \omega_e$ (so $\tilde{B}_1 = B$):

$$Q(s) = s + B, \quad (\text{D7})$$

$$P(s) = s^2 + Bs + A. \quad (\text{D8})$$

The two roots are $s_{\pm} = -B/2 \pm \sqrt{B^2/4 - A}$. Defining $b = \sqrt{A - B^2/4}$, the residue formula (D6) yields

$$C_{e0}(t) = e^{-Bt/2} \left[\cos(bt) + \frac{B}{2b} \sin(bt) \right], \quad (\text{D9})$$

which is Eq. (9).

3. Extension to arbitrary n

The construction generalizes directly to arbitrary n : the denominator $P(s)$ is always a polynomial of degree $n + 1$, and the solution is a sum of $n + 1$ exponentials with complex frequencies determined by its roots. For the kernel fits used in this work ($n = 7$ for the bare sphere, $n = 8$ for the core-shell), the roots are obtained numerically. Because the fully converged near-field multipole sums utilized in this work yield positive amplitudes, the Lorentzian decompositions function as exact, positive-definite pseudo-mode expansions. The physical requirement that $|C_{e0}(t)|^2 \leq 1$ and $\text{Re}(s_m) < 0$ for all poles is enforced natively by the positivity of the exact kernel spectrum $\mathcal{K}(\omega) \geq 0$.

[1] P. Törmä and W. L. Barnes, *Rep. Prog. Phys.* **78**, 013901 (2015).

[2] F. J. Garcia-Vidal, C. Ciuti, and T. W. Ebbesen, *Science* **373**, eabd0336 (2021).

- [3] D. G. Baranov, M. Wersäll, J. Cuadra, T. J. Antosiewicz, and T. Shegai, *ACS Photonics* **5**, 24 (2018).
- [4] A. González-Tudela, A. Reiserer, J. J. García-Ripoll, and F. J. García-Vidal, *Nat. Rev. Phys.* **6**, 166 (2024).
- [5] O. Bitton, S. N. Gupta, and G. Haran, *Nanophotonics* **8**, 559 (2019).
- [6] K.-D. Park, M. A. May, H. Leng, J. Wang, J. A. Kropp, T. Gougousi, M. Pelton, and M. B. Raschke, *Sci. Adv.* **5**, eaav5931 (2019).
- [7] R. Chikkaraddy, B. de Nijs, F. Benz, S. J. Barrow, O. A. Scherman, E. Rosta, A. Demetriadou, P. Fox, O. Hess, and J. J. Baumberg, *Nature* **535**, 127 (2016).
- [8] K. Santhosh, O. Bitton, L. Chuntunov, and G. Haran, *Nat. Commun.* **7**, 11823 (2016).
- [9] T. Neuman, R. Esteban, D. Casanova, F. J. García-Vidal, and J. Aizpurua, *Nano Letters* **18**, 2358 (2018), pMID: 29522686.
- [10] J. Fregoni, T. S. Haugland, S. Pipolo, T. Giovannini, H. Koch, and S. Corni, *Nano Letters* **21**, 6664 (2021).
- [11] P. Anger, P. Bharadwaj, and L. Novotny, *Phys. Rev. Lett.* **96**, 113002 (2006).
- [12] A. Trügler and U. Hohenester, *Phys. Rev. B* **77**, 115403 (2008).
- [13] A. Delga, J. Feist, J. Bravo-Abad, and F. J. Garcia-Vidal, *Phys. Rev. Lett.* **112**, 253601 (2014).
- [14] M. Pelton, *Nat. Photonics* **9**, 427 (2015).
- [15] J. B. Khurgin, *Nature Nanotechnology* **10**, 2 (2015).
- [16] N. T. Fofang, T.-H. Park, O. Neumann, N. A. Mirin, P. Nordlander, and N. J. Halas, *Nano Lett.* **8**, 3481 (2008).
- [17] N. T. Fofang, N. K. Grady, Z. Fan, A. O. Govorov, and N. J. Halas, *Nano Lett.* **11**, 1556 (2011).
- [18] M. Wersäll, J. Cuadra, T. J. Antosiewicz, S. Balci, and T. Shegai, *Nano Lett.* **17**, 551 (2017).
- [19] G. P. Wiederrecht, G. A. Wurtz, and J. Hranisavljevic, *Nano Lett.* **4**, 2121 (2004).
- [20] M. S. Rider, R. Arul, J. J. Baumberg, and W. L. Barnes, *Nanophotonics* **11**, 3695 (2022).
- [21] T. J. Antosiewicz, S. P. Apell, and T. Shegai, *ACS Photonics* **1**, 454 (2014).
- [22] S. Y. Buhmann, *Dispersion Forces I: Macroscopic Quantum Electrodynamics and Ground-State Casimir, Casimir-Polder and van der Waals Forces* (Springer, Berlin, 2012).
- [23] J. Feist, A. I. Fernández-Domínguez, and F. J. García-Vidal, *Nanophotonics* **10**, 477 (2021).
- [24] R. Sáez-Blázquez, Á. Cuartero-González, J. Feist, F. J. García-Vidal, and A. I. Fernández-Domínguez, *Nano Letters* **22**, 2365 (2022).
- [25] F. Herrera and J. Owrutsky, *The Journal of Chemical Physics* **152**, 100902 (2020).
- [26] F. Herrera and W. L. Barnes, *Philosophical Transactions of the Royal Society A: Mathematical, Physical and Engineering Sciences* **382**, 20230343 (2024).
- [27] A. S. Rema, A. E. Rubio López, and F. Herrera, arXiv:2509.03428 (2025), arXiv:2509.03428 [quant-ph].
- [28] I. Medina, F. J. García-Vidal, A. I. Fernández-Domínguez, and J. Feist, *Phys. Rev. Lett.* **126**, 093601 (2021).
- [29] S. Scheel and S. Y. Buhmann, *Acta Phys. Slovaca* **58**, 675 (2008).
- [30] S. Wang, G. D. Scholes, and L.-Y. Hsu, *J. Chem. Phys.* **151**, 014105 (2019).
- [31] F. Lindel, D. Lentrodt, S. Y. Buhmann, and C. Schäfer, *J. Chem. Phys.* **161**, 154111 (2024).
- [32] W. C. Chew, *Waves and Fields in Inhomogeneous Media* (Wiley-IEEE Press, 1999).
- [33] J. E. Sipe, *Phys. Rev. A* **52**, 1875 (1995).
- [34] M. V. Fedorov, M. A. Efremov, A. E. Kazakov, K. W. Chan, C. K. Law, and J. H. Eberly, *Phys. Rev. A* **72**, 032110 (2005).
- [35] A. S. Leathers and D. A. Micha, *Chem. Phys. Lett.* **415**, 46 (2005).
- [36] A. D. Polyandin and A. V. Manzhirrov, *Handbook of Integral Equations*, 2nd ed. (CRC Press, 2008).
- [37] P. R. Berman and G. W. Ford, in *Advances in Atomic, Molecular, and Optical Physics*, Vol. 59 (Academic Press, 2010) pp. 175–221.
- [38] B. M. Garraway, *Phys. Rev. A* **55**, 2290 (1997).
- [39] B. J. Dalton, S. M. Barnett, and B. M. Garraway, *Phys. Rev. A* **64**, 053813 (2001).
- [40] S. Franke, S. Hughes, M. K. Dezfouli, P. T. Kristensen, K. Busch, A. Knorr, and M. Richter, *Phys. Rev. Lett.* **122**, 213901 (2019).
- [41] S. Savasta, R. Saija, A. Ridolfo, O. Di Stefano, P. Denti, and F. Borghese, *ACS Nano* **4**, 6369 (2010).
- [42] C. Van Vlack, P. T. Kristensen, and S. Hughes, *Phys. Rev. B* **85**, 075303 (2012).
- [43] A. E. Schlather, N. Large, A. S. Urban, P. Nordlander, and N. J. Halas, *Nano Lett.* **13**, 3281 (2013).
- [44] G. Zengin, M. Wersäll, S. Nilber, T. J. Antosiewicz, M. Käll, and T. Shegai, *Phys. Rev. Lett.* **114**, 157401 (2015).
- [45] M. S. Rider, E. C. Johnson, D. Bates, W. P. Wardley, R. H. Gordon, R. D. J. Oliver, S. P. Armes, G. J. Leggett, and W. L. Barnes, *Nanophotonics* **13**, 2453 (2024).
- [46] C. Schneider, M. M. Glazov, T. Korn, S. Höfling, and B. Urbaszek, *Nature Communications* **9**, 2695 (2018).
- [47] A. Fieramosca, L. Polimeno, V. Ardizzone, L. D. Marco, M. Pugliese, V. Maiorano, M. D. Giorgi, L. Dominici, G. Gigli, D. Gerace, D. Ballarini, and D. Sanvitto, *Science Advances* **5**, eaav9967 (2019).
- [48] E. Prodan, C. Radloff, N. J. Halas, and P. Nordlander, *Science* **302**, 419 (2003).
- [49] D. Gülen, *The Journal of Physical Chemistry B* **117**, 11220 (2013).
- [50] G. Mie, *Ann. Phys.* **330**, 377 (1908).
- [51] C. F. Bohren and D. R. Huffman, *Absorption and Scattering of Light by Small Particles* (John Wiley & Sons, New York, 1983).
- [52] L.-W. Li, P.-S. Kooi, M.-S. Leong, and T.-S. Yee, *IEEE Trans. Microw. Theory Tech.* **42**, 2302 (1994).
- [53] J. Hakami, L. Wang, and M. S. Zubairy, *Phys. Rev. A* **89**, 053835 (2014).
- [54] A. Cuartero-González and A. I. Fernández-Domínguez, *ACS Photonics* **5**, 3415 (2018).
- [55] W. J. Tan, P. A. Thomas, I. J. Luxmoore, and W. L. Barnes, *The Journal of Chemical Physics* **154**, 024704 (2021).
- [56] A. Kuzyk, R. Schreiber, Z. Fan, G. Pardatscher, E.-M. Roller, A. Högele, F. C. Simmel, A. O. Govorov, and T. Liedl, *Nature* **483**, 311 (2012).
- [57] J. Yang, N. Xu, K. Liu, W. Song, and J.-H. Zhong, *Advances in Physics: X* **11**, 2628526 (2026).
- [58] F. Herrera and F. C. Spano, *Phys. Rev. Lett.* **116**, 238301 (2016).

- [59] D. Wellnitz, G. Pupillo, and J. Schachenmayer, *The Journal of Chemical Physics* **154**, 054104 (2021).
- [60] W. Ying and A. Nitzan, *The Journal of Chemical Physics* **164**, 024113 (2026).
- [61] Á. Buendía, J. A. Sánchez-Gil, V. Giannini, W. L. Barnes, and M. S. Rider, *Nanophotonics* **13**, 4555 (2024).
- [62] K. Bedingfield, B. Yuen, and A. Demetriadou, *Phys. Rev. B* **111**, 075420 (2025).
- [63] C.-T. Tai, *Dyadic Green's Functions in Electromagnetic Theory* (Intext Educational Publishers, Scranton, PA, 1971).
- [64] T. J. Arruda, A. S. Martínez, and F. A. Pinheiro, *Phys. Rev. A* **96**, 013834 (2017).